

# Simultaneous Identification of Low and High Atomic Number Atoms in Monolayer 2D Materials Using 4D Scanning Transmission Electron Microscopy

Yi Wen,<sup>†</sup> Colin Ophus,<sup>‡</sup> Christopher S. Allen,<sup>†,§</sup> Shiang Fang,<sup>⊥</sup> Jun Chen,<sup>†</sup> Efthimios Kaxiras,<sup>⊥,¶</sup> Angus I. Kirkland,<sup>†,§</sup> and Jamie H. Warner<sup>\*,†,¶</sup>

<sup>†</sup>Department of Materials, University of Oxford, Parks Road, Oxford OX1 3PH, United Kingdom

<sup>‡</sup>National Center for Electron Microscopy, Molecular Foundry, Lawrence Berkeley National Laboratory, 1 Cyclotron Road, Berkeley, California 94720, United States

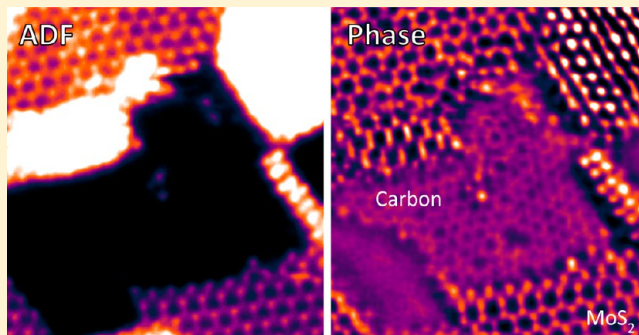
<sup>§</sup>Electron Physical Sciences Imaging Center, Diamond Light Source Ltd., Didcot, Oxfordshire OX11 0DE, United Kingdom

<sup>⊥</sup>Department of Physics and <sup>¶</sup>John A. Paulson School of Engineering and Applied Sciences, Harvard University, Cambridge, Massachusetts 02138, United States

## Supporting Information

**ABSTRACT:** Simultaneous imaging of individual low and high atomic number atoms using annular dark field scanning transmission electron microscopy (ADF-STEM) is often challenging due to substantial differences in their scattering cross sections. This often leads to contrast from only the high atomic number species when imaged using ADF-STEM such as the Mo and 2S sites in monolayer MoS<sub>2</sub> crystals, without detection of lighter atoms such as C, O, or N. Here, we show that by capturing an array of convergent beam electron diffraction patterns using a 2D pixelated electron detector (2D-PED) in a 4D STEM geometry enables identification of individual low and high atomic number atoms in 2D materials by multicomponent imaging. We have used ptychographic phase reconstructions, combined with angular dependent ADF-STEM reconstructions, to image light elements at lateral (nanopores) and vertical interfaces (surface dopants) within 2D monolayer MoS<sub>2</sub>. Differential phase contrast imaging (Div(DPC)) using quadrant segmentation of the 2D pixelated direct electron detector data not only qualitatively matches the ptychographic phase reconstructions in both resolution and contrast but also offers the additional potential for real time display. Using 4D-STEM, we have identified surface adatoms on MoS<sub>2</sub> monolayers and have separated atomic columns with similar total atomic number into their relative combinations of low and high atomic number elements. These results demonstrate the rich information present in the data obtained during 4D-STEM imaging of ultrathin 2D materials and the ability of this approach to extract unique insights beyond conventional imaging.

**KEYWORDS:** MoS<sub>2</sub>, 4D STEM, amorphous carbon, adatom, ptychographic phase reconstruction, low angle annular dark field



In the past decade, 2D transition metal dichalcogenides (TMDs), including MoS<sub>2</sub> and WS<sub>2</sub>, have shown potential use in ultrathin electronic devices due to their tunable band structure, flexibility, transparency, and scalable production using chemical vapor deposition (CVD) methods.<sup>1–3</sup> These materials form atomically thin crystals with surface areas up to the centimeter scale, making them suitable for applications that require a large specific surface area. This includes, for example, loading of catalytically active particles, edge-decorated and surface-bound functional groups for sensors, and the use of nanopores in a membrane for desalination and DNA translocation.<sup>4–8</sup> The latter nanopores in 2D crystals can be created by electrochemical reactions, oxygen plasma etching, ion beam irradiation, and in situ electron beam engineering.<sup>9–15</sup> However, even under the high vacuum conditions in the electron microscope, 2D materials are often covered with

some amount of amorphous carbon surface residue arising from the organic solvents and polymers used in the processing, or by impurity atmospheric adsorbates. Importantly, if a nanopore is completely blocked, it is no longer useful, and if a nanopore is only partially blocked, this will reduce the nanopore size giving rise to a different behavior when used as a separation membrane. Therefore, the ability to image both low atomic number elements such as carbon, as well as high atomic number elements such as Mo or W in TMDs, is essential for future nanopore design in TMD materials.

**Received:** July 4, 2019

**Revised:** August 12, 2019

**Published:** August 20, 2019



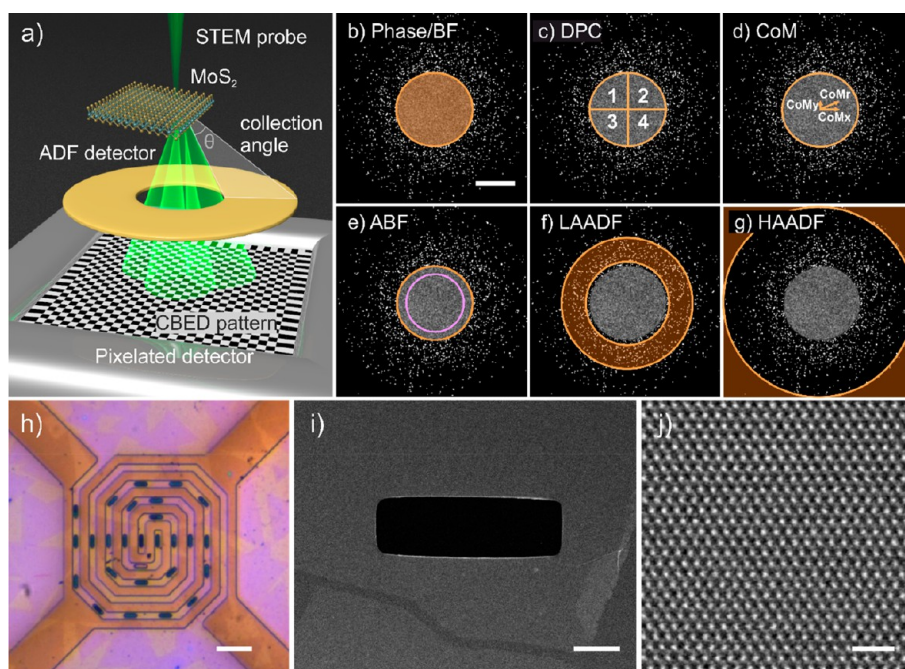


**Figure 1.** (a) Schematic of 4D-STEM data acquisition. (b–g) Various reconstructions from a 4D data set, superimposed on a ED pattern, where the circles indicate virtual detector inner and outer collection angles and shadowed regions indicate summed areas. BF: bright field. DPC: differential phase contrast. CoM: center of mass. ABF: annular bright field. LAADF: low angle annular dark field. HAADF: high angle annular dark field. Scale bar indicates 40 mrad. (h) Optical image of CVD-grown MoS<sub>2</sub> (purple triangular-shaped domains) on an in situ heating chip. Scale bar indicates 40  $\mu$ m. (i) ADF-STEM image of a MoS<sub>2</sub> crystal covering a slit on a Si<sub>3</sub>N<sub>4</sub> support film. Scale bar indicates 1  $\mu$ m. (j) ADF-STEM image of a monolayer MoS<sub>2</sub> lattice. Scale bar indicates 1 nm.

Annular dark field scanning transmission electron microscopy (ADF-STEM) has been used extensively to discriminate metal and chalcogen atom columns and to provide structure details of S vacancies and edge terminations in 2D TMDs. However, it is challenging to simultaneously image light atoms in the presence of heavy ones using this geometry. Bright field phase contrast imaging is sensitive to the presence of light atoms, but the intensity is strongly dependent on specimen thickness and inner electrostatic potential. For these reasons, phase contrast images are often not easily interpreted and generally rely on postacquisition image simulation against various experimental parameters and structural models.

Collecting far field electron diffraction (ED) patterns from a set of STEM probe positions using a fast 2D pixelated direct electron detector (2D-PED) allows the recording of data sets suitable for both ptychographic and ADF-STEM reconstruction simultaneously. This requires the 2D-PED to have fast-readout and high dynamic range with single electron sensitivity.<sup>16,17</sup> Figure 1a shows the geometry of a typical 4D STEM data acquisition in which the 2D-PED operates in conjunction with an ADF detector. The benefit of capturing the full ED pattern is that it allows various postacquisition reconstructions (Figure 1b–g) including bright field (BF), annular bright field (ABF), annular dark field (ADF), electric field maps, phase retrieval (ptychography), differential phase contrast (DPC), and integrated differential phase contrast (iDPC). In turn, this wide variety of signals that can be synthesized enables the construction of interpretable elemental maps, which are essential for differentiating sublattice sites, vacancies and dopants, and the local projected electric field, giving insight into the local electrostatic properties.<sup>18–21</sup> Phase contrast images, which have been used extensively in both optical and transmission electron microscopy, represent the

local projected potential. Ptychographic phase reconstruction has been successfully applied using various algorithms including Wigner distribution deconvolution (WDD)<sup>22–24</sup> and extended phase iterative engines (ePIE).<sup>25</sup>

The 4D STEM geometry has recently been used to study various materials including single Au atoms, SrTiO<sub>3</sub>, DyScO<sub>3</sub>, GaN, graphene, and MoS<sub>2</sub>.<sup>17,21,26–29</sup> However, the correlation of the CoM shift and projected electric field requires a specimen thickness of  $\sim 1$ –2 nm, and therefore, 2D materials are intrinsically suitable for studies using this technique. For the specific case of TMDs, 4D STEM can be used to monitor tunable electronic properties as a function of stacking, doping, electron beam induced defect formation, and in situ heating and biasing (Figure 1h–j). In this paper, we demonstrate the use of 4D STEM for imaging light elements in form of carbon surface adatoms and monolayer films within TMDs, providing the possibility for real-time imaging of defect evolution based on differential phase contrast.

**Results and Discussion.** Surface carbon residues are typically found on all 2D materials and can further increase locally during STEM imaging.<sup>30</sup> This carbon-based contamination is either due to residue from the transfer process (organic solvent) or from the microscope vacuum. There is some evidence from previous studies to suggest that the latter is important, where it was shown that surface carbon redeposits on samples subject to heating and subsequent cooling in the TEM vacuum.<sup>31,32</sup> Figure 2a shows a typical image of MoS<sub>2</sub> with monolayer regions of surface carbon adsorbate. Two nanopores have been drilled in this region using the STEM probe. However, it is hard to detect if the amorphous carbon covers these nanopores or if they are open. For pores that are partially covered (Figures 2b,c), the amorphous carbon within the pores shows slightly higher intensity than the vacuum. In



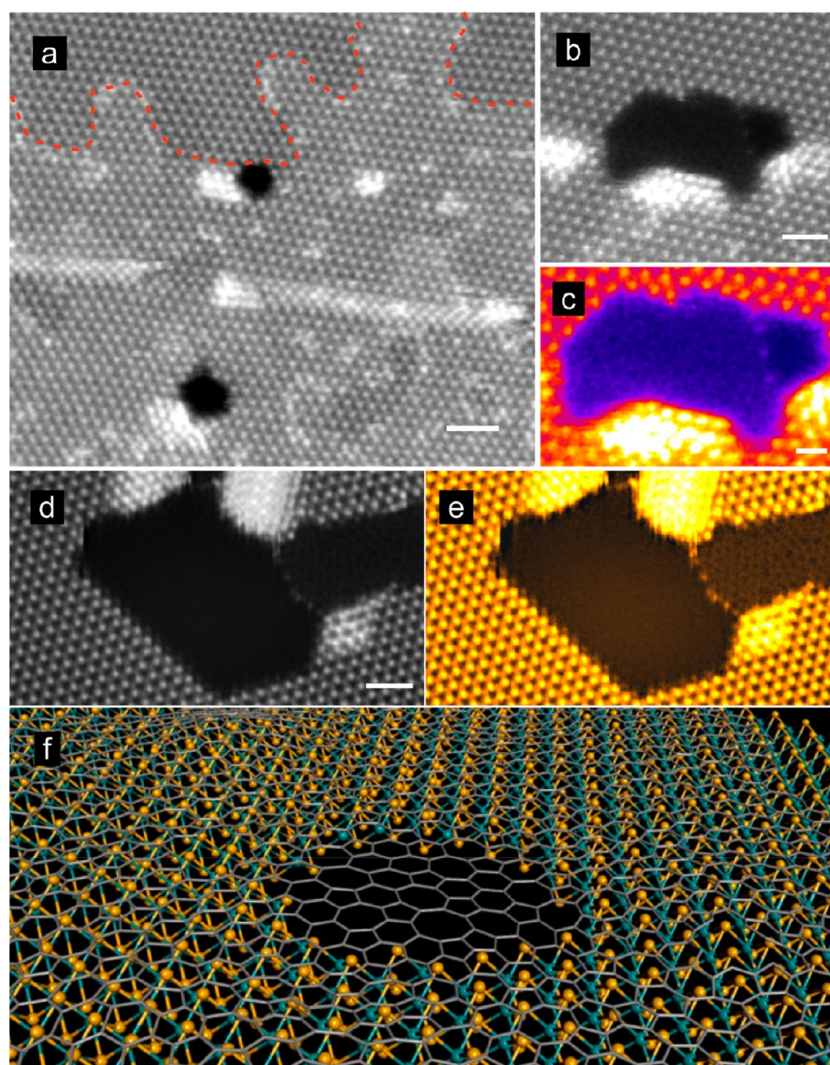


**Figure 2.** Low-magnification ADF-STEM images of MoS<sub>2</sub> with carbon contamination. (a) Drilled nanopores surrounded by amorphous carbon contamination. To aid visualization, regions with carbon (higher contrast) are delineated from clean regions by red dotted lines. The convergence semiangle used was 31.5 mrad, camera length 16 cm, detector collection angle 49.5–198 mrad, probe size estimated to be 1.9 Å. (b) Nanopore partially covered with a carbon layer and (c) magnified view of this pore in false color showing internal atoms. (d) Multiframe ADF-STEM images showing a nanopore partially covered with a carbon layer and (e) the same region displayed with false color, for visualization of the carbon lattice. (f) Schematic 3D view of surface carbon covering a nanopore in MoS<sub>2</sub>. For panels a, b, d, and e, the scale bar indicates 1 nm; for panel c, the scale bar indicates 0.5 nm.

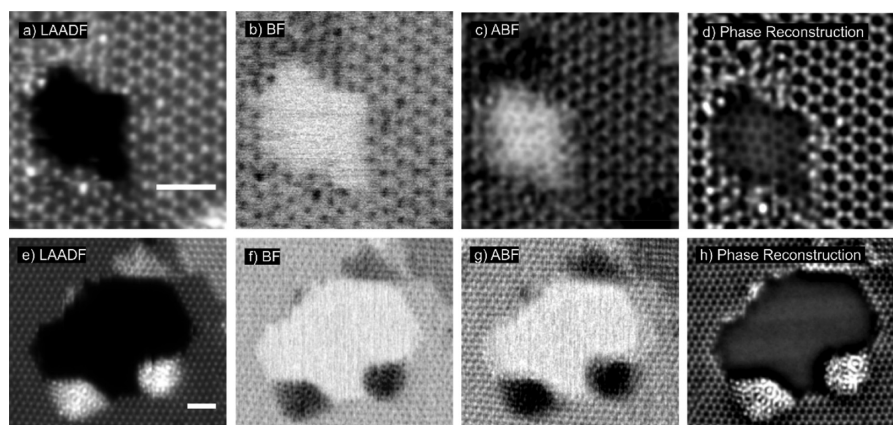
addition, multiframe averaging helps to resolve the carbon lattice because of the improved signal-to-noise (Figures 2d,e). Figure 2f shows a schematic illustration of a nanopore in MoS<sub>2</sub> covered with carbon monolayer.

Figure 3 shows reconstructions from 4D data sets of MoS<sub>2</sub> and WS<sub>2</sub> with nanopores (reconstruction details are given in the Supporting Information). In the reconstructed low angle ADF (LAADF) images (Figure 3a,e), both lattices are clearly resolved with atomic sites in bright contrast and regions inside the holes as dark contrast. Reconstructed BF images (Figure 3b,f) show reversed contrast but provide similar information. However, in the reconstructed ABF image, regular features are observed inside the MoS<sub>2</sub> hole (Figure 3b), which are more pronounced in the reconstructed phase (Figure 3d). In contrast, the WS<sub>2</sub> hole (Figure 3h) is apparently clean.

The structure visible within the MoS<sub>2</sub> nanopore is due to residual surface carbon and is confirmed by measuring the bond length (0.15 nm) using the MoS<sub>2</sub> lattice as a reference

(Figure 4a), which gives a value close to that for a C–C bond in a hexagonal carbon ring (0.14 nm). A similar defective carbon monolayer lattice has also been observed in a conventional aberration corrected phase contrast TEM image (Figure 4g). Multislice simulations of the reconstructed phase (Figure 4b)<sup>33,34</sup> qualitatively agree with the experimental data (Figure 4a) as do the ABF reconstructions, which also show sensitivity to light elements, but they fail to reach sufficient resolution at low magnification (Figure S1).<sup>35</sup> Simulations of the BF, ABF, and div(DPC) are shown in Figure 4d–f. The div(DPC) simulation, Figure 4f, shows simultaneous imaging of both the carbon lattice and the MoS<sub>2</sub>, with phase values qualitatively similar to those in the reconstructed phase shown in Figure 4b.

In Figure 5, we examine regions where the carbon monolayer films are on the surface and also where they bond directly to the edge of the MoS<sub>2</sub> (Figure S2). The ptychographic reconstructed phase image, Figure 5a, shows



**Figure 3.** 4D STEM reconstructed data recorded at 700 °C from (a–d) MoS<sub>2</sub> and (e–h) WS<sub>2</sub> both with a hole. For MoS<sub>2</sub>, the convergence semiangle used was 39.1 mrad, camera length 6 cm, probe size estimated to be 1.5 Å. (a) LAADF reconstructed using a 40–60 mrad collection angle, (b) BF using a 0–39 mrad collection angle, (c) ABF using a 27–39 mrad collection angle. For WS<sub>2</sub>, a convergence of 30.6 mrad was used, camera length 6 cm, probe size estimated to be 1.9 Å. (e) LAADF reconstructed using a 40–60 mrad collection angle, (f) BF using a 0–30 mrad collection angle, (g) ABF using a 30 mrad collection angle. Scale bar indicates 1 nm and applies to panels a–c and d–f, respectively.

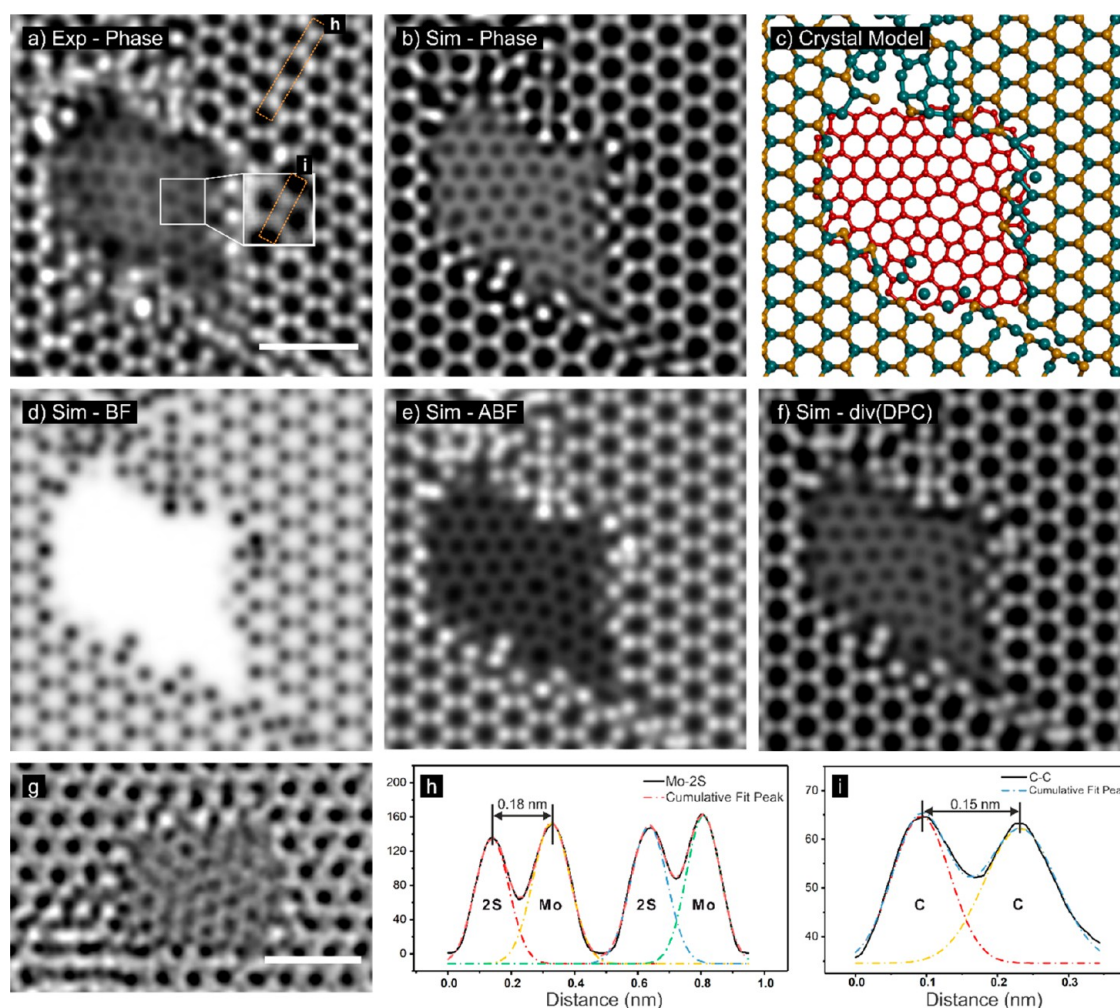


**Figure 4.** (a) Reconstructed ptychographic phase from 4D STEM data. (b) Multislice simulation of the reconstructed phase based on the atomic model in panel c. (c) Crystal model. (d–f) Multislice simulations of BF, ABF, and div(DPC) based on the atomic model in panel c. (g) Bright field phase contrast TEM image of a nanopore in MoS<sub>2</sub> filled with a defective carbon monolayer. (h) Line profile of the intensity taken from the boxed region indicated in panel a, fitted with Gaussian functions to locate the peak centers used to measure the Mo–2S distance. (i) Line profile taken from the boxed region indicated in panel a with the C–C distance measured. All the scale bars indicate 1 nm. Convergence semiangle is 39.1 mrad, camera length 6 cm, probe size estimated to be 1.5 Å.



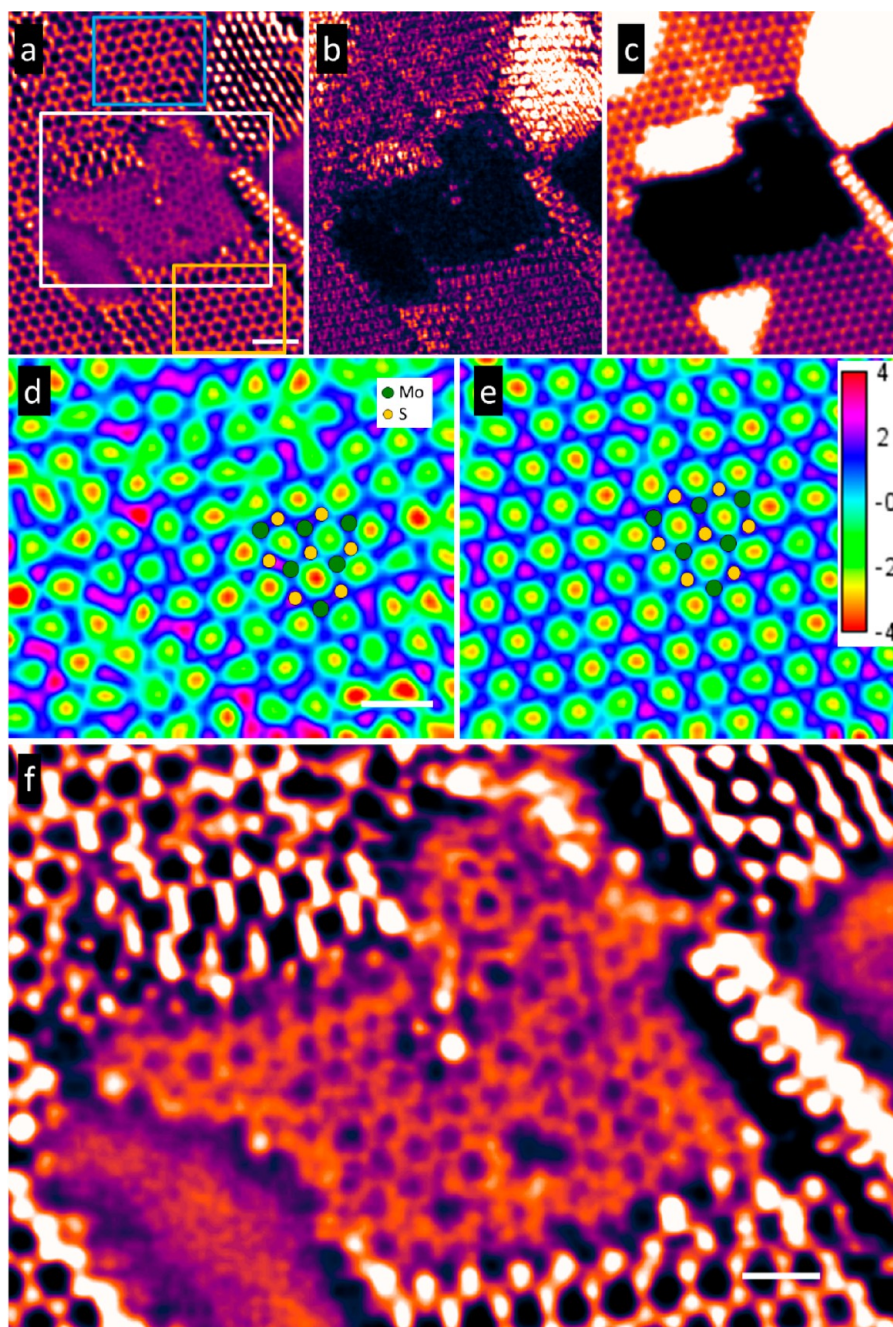


**Figure 5.** (a) Ptychographic phase image and (b) CoM shift of a carbon monolayer bridge across a gap in MoS<sub>2</sub> reconstructed from the same data set and (c) simultaneous HAADF image. False color gem LUT was used for better contrast. (d, e) Zoomed-in regions in blue and yellow boxes in panel a, respectively, using false color LUT spectrum to visualize the uneven and random distribution of carbon on MoS<sub>2</sub> in panel c, which caused distortion in phase image, and the clean MoS<sub>2</sub> in panel d. (f) Zoomed-in region in white box in panel a, showing detailed information on the carbon bonded with MoS<sub>2</sub> lattice. Scale bar in panel a indicates 1 nm and applies to panels b and c. Scale bars in panel d indicate 0.5 nm and apply to panel e. Scale bar in panel f indicates 0.5 nm. Convergence semiangle is 30.6 mrad, camera length 20 cm, probe size estimated to be 1.9 Å.

the carbon and MoS<sub>2</sub> lattices together, while the CoM shift map, Figure 5b, shows uniformity of the MoS<sub>2</sub> signal in the bottom section (yellow box) indicating it is free from surface carbon in this area. The top section of MoS<sub>2</sub>, (blue box) shows signal variations that are due to randomly orientated disordered carbon on the surface. This is seen more clearly in Figure 5d and e, where the two regions are compared. The simultaneous HAADF image, Figure 5c, enables the position of Mo and S sites to be determined due to Mo having higher

signal than S. The high-magnification image in Figure 5f reveals the carbon bonding directly to the Mo rich edge.

The divergence of the center of mass shift ( $\text{div}(\text{CoM})$ ) is also capable of resolving the carbon lattice. The DPC and CoM shifts share some similarities as they both quantify the distribution of the electrons inside the BF disk and can be directly related to the local electromagnetic field.<sup>36</sup> Thus,  $\text{div}(\text{DPC})$  and CoM shift are linearly related to the local charge density through Poisson's equation,<sup>21</sup> whereas the reconstructed phase is related to the projected electrostatic

potential and is an indication of local charge distribution. Hence, both yield a qualitative charge density map, as shown in Figure 6c and d. The image in Figure 6d can be computed significantly faster than the phase reconstruction, and this opens up the possibility for real time display.

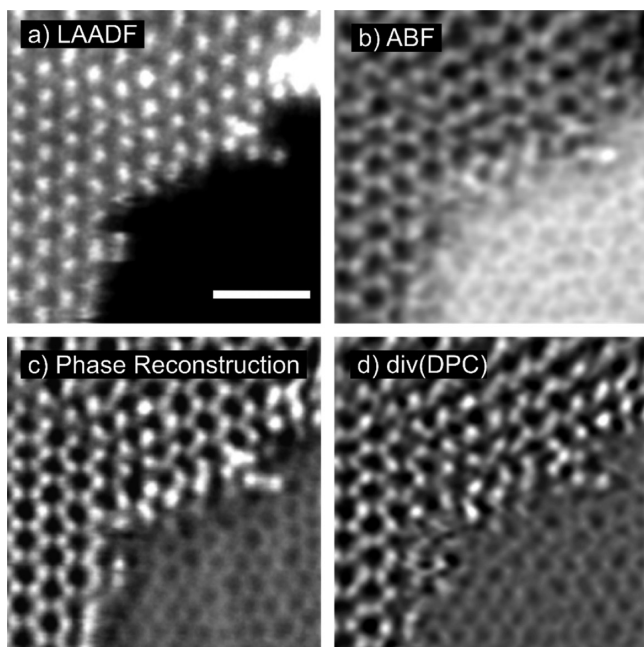


**Figure 6.** Nanopore in  $\text{MoS}_2$  filled with a carbon layer reconstructed from 4D STEM data. (a) LAADF reconstructed using a 40–60 mrad collection angle. (b) ABF using a 27–39 mrad collection angle. (c) Ptychographic reconstruction of the phase. (d) Div(DPC). Scale bar indicates 1 nm and applies to Panels a–d. Convergence semiangle is 39.1 mrad, camera length 6 cm, probe size estimated to be 1.5 Å.

Next we examine light atoms on the surface of TMDs. High angle annular dark field (HAADF) STEM imaging shows contrast that is quantitative in  $Z$  if the collection angle is sufficiently high. However, this makes the imaging of light atoms challenging, especially in the presence of heavy elements. To overcome this while maintaining high resolution, LAADF-STEM has been used extensively in detecting defect structures, for example, oxygen vacancies in  $\text{SrTiO}_3$ ,  $\text{Ce}^{3+}$  in  $\text{CeO}_2$ , light dopants, and vacancies with depth sensitivity in the presence of strain contrast.<sup>37–41</sup>

4D STEM is ideal for exploring the angular dependence of ADF image contrast as capturing the whole ED pattern allows postacquisition reconstruction. From Figure 7a, it can be seen that for monolayer  $\text{MoS}_2$ , an extra atom is located at a 2S site, most likely as a surface adatom or dopant and appears brighter in the reconstructed LAADF image than the adjacent Mo atom. However, the intensity at this site intensity drops significantly with increasing detector angular range (Figures S3b–e) until it is not detected under HAADF conditions (Figure 7b). The presence of such an adatom is also not obvious in the reconstructed phase (Figure 7c), where the column shows only slightly higher contrast.

Other bright adatoms/dopants have been observed in LAADF images at both the 2S site (Figure 8a) and Mo site (Figure 9a). However, in these images, the difference in contrast varies less as a function of increasing collection angle (Figures S4 and S5), suggesting different adatom species to

those shown in Figure 7. To understand this, we have simulated images of structures with both light surface adatoms including C, N, and O, which are common contaminants inside the microscope column, and heavy surface adatoms. Figure 7e,f and Figure S3g–l show simulations of a C adatom sitting on top of a 2S site demonstrating good qualitative agreement with the experimental data (Figures 7i,j), in which the site of the adatom adsorption exhibits lower contrast compared to the Mo atom under HAADF conditions but higher contrast under LAADF conditions. For the second case where a O adatom is located on top of a Mo atom (Figure 8), the experimental and simulated data show that the HAADF contrast never drops below that due to a single Mo site, but under LAADF conditions, the contrast increases significantly. Finally, for the third case where a heavy adatom sits on top of a heavy Mo atom (Figures 9 and S5), the experimental and simulated data show that the contrast from the adatom site is always higher than that due to a single Mo atom under both LAADF and HAADF conditions. Overall, these three cases show that it is possible to use 4D STEM and the angular dependency of the LAADF/MAADF conditions to discriminate atomic columns with light–light, light–heavy, and heavy–heavy adatom combinations. High angle annular dark field (HAADF) imaging provides quantitative analysis when the collection angle is sufficiently high (for inner collection angle  $\beta_{\text{in}} > 3\alpha$ ) because the electrons in this angular range are incoherently and elastically scattered by the atomic nucleus. This gives rise to a HAADF signal intensity that has nonlinear dependence on the atomic number ( $I \approx Z^{1.7}$ ). At low scattering angles, the signals are produced by more complex scattering mechanisms, and the intensity can no longer be simply expressed as a power law function of  $Z$ .

Finally, we have explored the potential for local electric field (EF) imaging around atoms reconstructed from 4D STEM data to differentiate adatoms on TMDs. Prior work on 4D STEM of  $\text{MoS}_2$  and  $\text{WS}_2$  has demonstrated EF imaging around single atoms and its sensitivity, showing the triangular patterns of signal located around the atomic nucleus.<sup>26,42</sup> The field drops to zero close to the midpoint between the Mo and 2S atoms. Figure 10a shows the 2D projected EF map of the adatom also shown in Figure 7, which is compared to density functional theory (DFT) calculated EF maps based on a carbon and an oxygen adatom, respectively (Figure 10b and c, DFT method described in the SI). Although the DFT results provide an accurate prediction of the shape and magnitude of the EF, they are unable to differentiate C and O adatoms, while on the basis of simulations ADF imaging can distinguish these (Figure S6). The difference between the DFT and experimental EF is likely due to scan distortion during acquisition that is hard to completely eliminate. Furthermore, two adatoms as seen in Figures 8 and 9 can be detected in ADF data (Figure 10e), and their respective low-magnification electric field maps are shown in Figure 10h, where the adatom site appears brighter compared to the equivalent lattice sites. However, analysis of the EF signals for these two adatoms, (Figure 10i,j) shows minimal difference, and they cannot be differentiated. This indicates that while EF is able to provide sufficient contrast to identify the presence of adatoms, it is unable to differentiate columns with similar total atomic numbers arising from different combinations of light and heavy atoms.

**Conclusions.** We have demonstrated the use of 4D STEM to reconstruct multiple imaging contrast methods for the



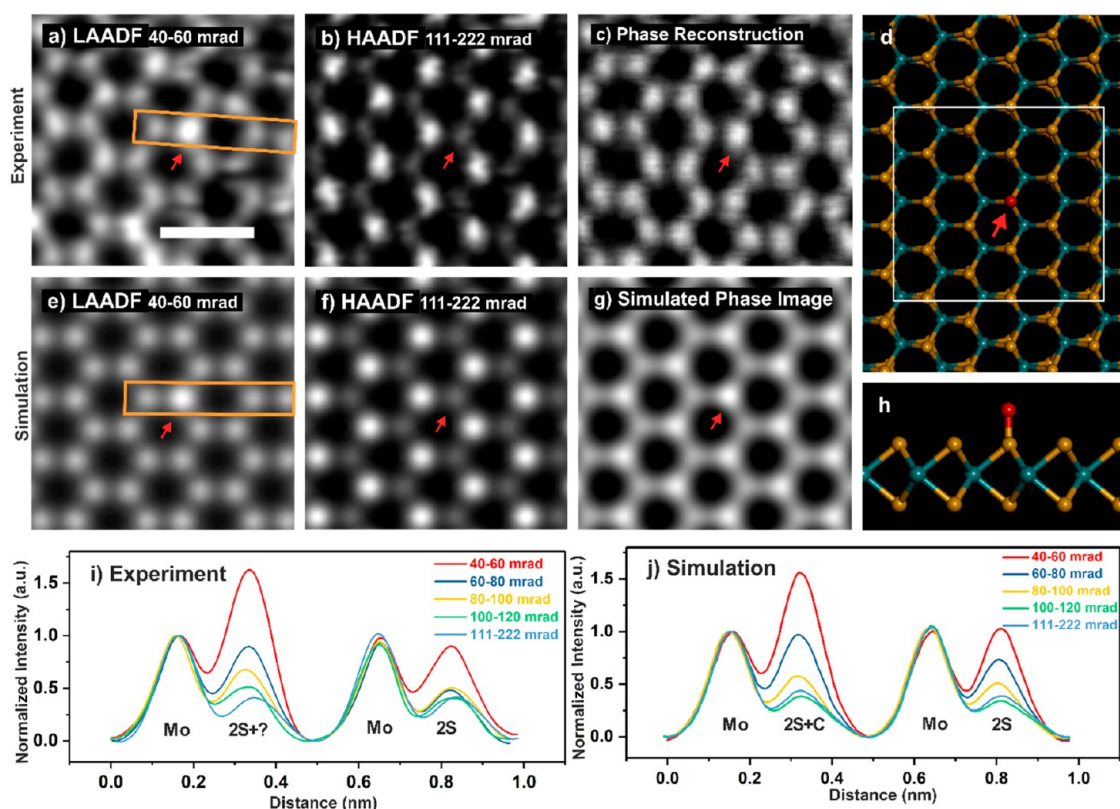


**Figure 7.** Surface adatom (indicated by red arrows) on 2S site in a  $\text{MoS}_2$  lattice. (a) LAADF reconstruction using a 40–60 mrad collection angle. (b) Simultaneous HAADF image. (c) Phase reconstruction (method in the SI). (d) Crystal model of a C adatom on 2S site where the red arrow indicates the adatom position. (e) Simulated LAADF and (f) HAADF images and (g) phase contrast image based on the boxed regions in the crystal model in panel d. (h) Side view of crystal model in panel d. (i) Line profiles of the boxed region in panel a and corresponding regions in panel b and Figure S3b–d (intensities were normalized to the peak intensity of the Mo atom). (j) Line profiles of the boxed region in the simulated ADF images in (e, f, and Figure S3h–j) (intensities were also normalized to the peak intensity of first Mo atom). (j) Side view of the model shown in panel d. Scale bar indicates 0.5 nm and applies to panels a–d. Convergence semiangle is 39.1 mrad, camera length 6 cm, probe size estimated to be 1.5 Å.

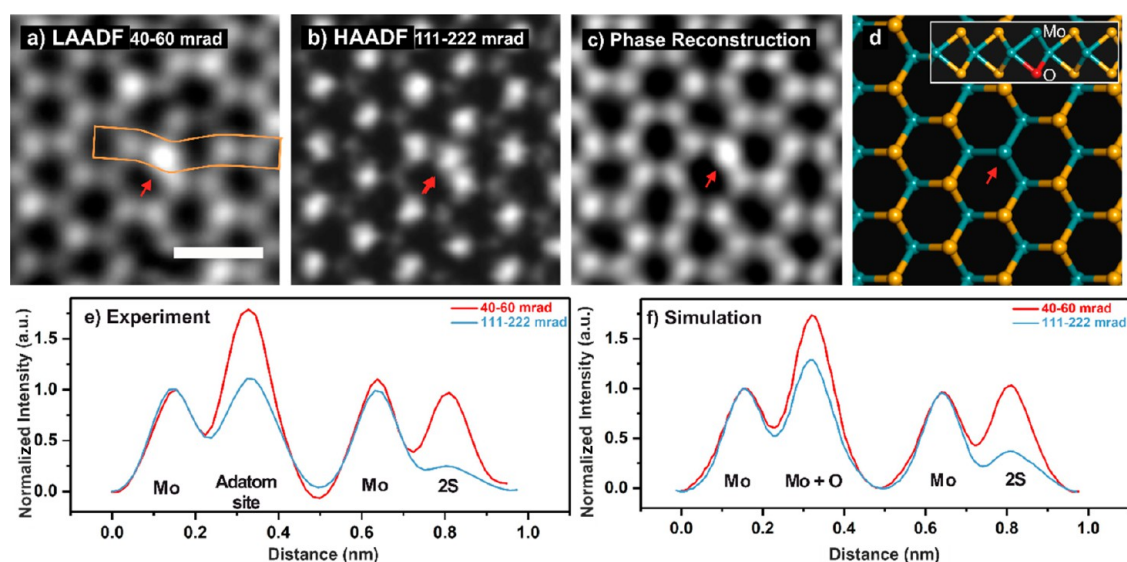


**Figure 8.** Surface adatom (indicated by red arrows) at a 2S site in  $\text{MoS}_2$  showing a different intensity trend compared to Figure 7. (a) Reconstructed LAADF image and (b) HAADF image with collection angles indicated. (c) Phase reconstruction. (d) Crystal model showing a Mo atom and a C atom at a 2S site with inset the side view of this model. (e) Line profiles from the boxed regions in panels a and b (normalized to the peak intensity of a Mo atom). (f) Line profiles of boxed regions shown in simulated ADF images (Figures S4f,j) (normalized to the peak intensity of a Mo atom) based on the crystal model in panel d. Convergence semiangle is 39.1 mrad, camera length 6 cm, probe size estimated to be 1.5 Å. Scale bar indicates 0.5 nm and applies to panels a–d.

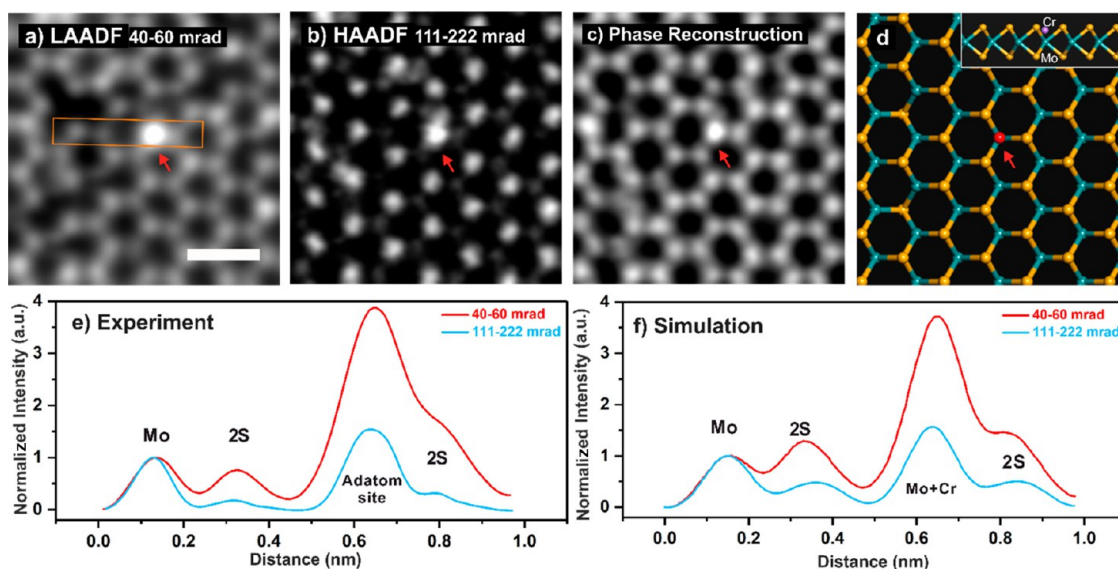


**Figure 9.** Surface adatom (indicated by red arrows) at a Mo site in  $\text{MoS}_2$  showing different intensity behavior comparing to the data in Figure 7. (a) Reconstructed LAADF image and (b) HAADF image with collection angles indicated. (c) Phase reconstruction. (d) Crystal model showing an adatom at a Mo site with inset the side view of this model. (e) Line profiles of boxed regions in panels a and b (normalized to the peak intensity of a Mo atom). (f) Line profiles of the boxed region shown in simulated ADF images (Figures S5f,j) (normalized to the peak intensity of a Mo atom) based on crystal model in panel d. Convergence semiangle is 39.1 mrad, camera length 6 cm, probe size estimated to be 1.5 Å. Scale bar indicates 0.5 nm and applies to panels a–d.

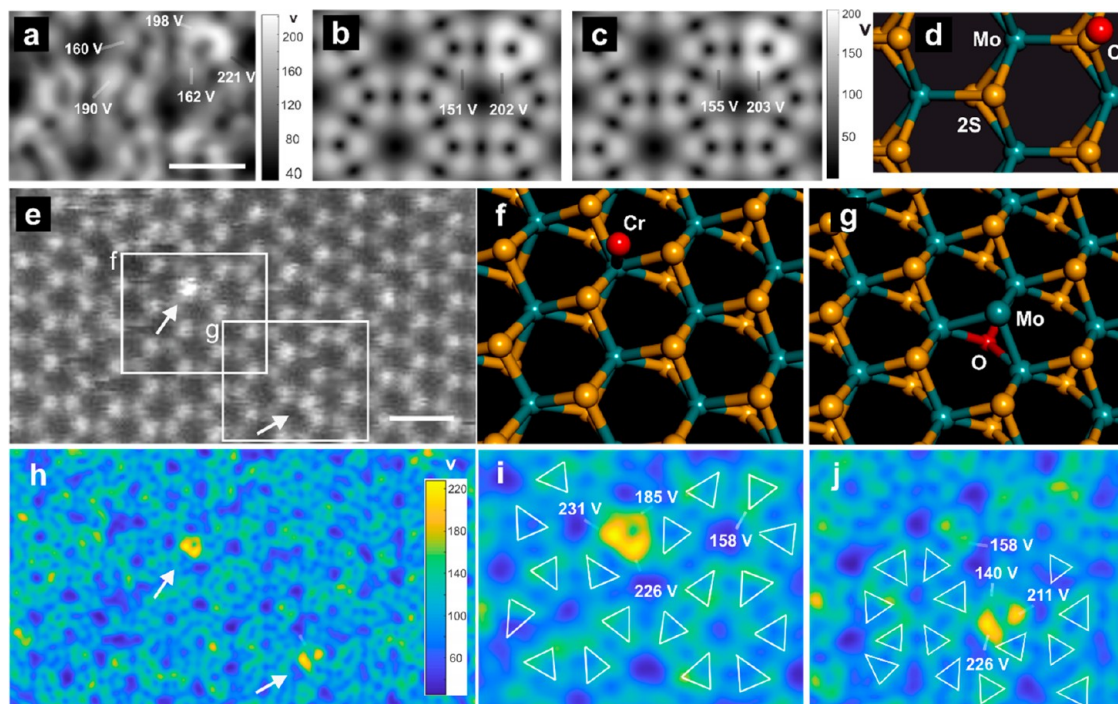


**Figure 10.** ADF images and electric field maps reconstructed from a 4D STEM data set compared with DFT calculations. The electric field maps were scaled to match the value from pristine area to that of DFT calculations. (a) Electric field map of a light adatom (described in Figure 7) at a 2S site compared with a DFT calculation of the electric field due to (b) carbon and (c) oxygen adatom on a 2S site, based on the model in panel d. Scale bar indicates 0.25 nm and applies to panels a–d. (e) ADF STEM image reconstructed with a 60–200 mrad collection angle. Scale bar indicates 0.5 nm and applies to panels e and h. (f, g) Models of the boxed regions in panel e. (h–j) Electric field maps corresponding to the marked region in panel e and to the models in panels f and g, respectively, with false color used to emphasize the higher EF intensities at adatom sites. The triangular shaped electric fields around each atom are indicated in panels i and j. Convergence semiangle is 39.1 mrad, camera length 6 cm, probe size estimated to be 1.5 Å.

detection and identification of single light and heavy atoms in 2D monolayer samples. Using ptychographic phase reconstructions, combined with LAADF, and HAADF images,

allows the detection of both light elements such as C atoms along with heavier Mo and W atoms. We have further showed how analysis of the angular dependent scattering can detect the



composition of surface adatom sites comprised of multiple elements of different atomic number. This imaging approach could be extended further to other interfaces that involve carbon materials and heavier elements. In addition, the ability to detect carbon filling of nanopores could assist in future studies of edges and nanopores for applications in membranes and other devices.

## ■ ASSOCIATED CONTENT

### ■ Supporting Information

The Supporting Information is available free of charge on the ACS Publications website at DOI: 10.1021/acs.nanolett.9b02717.

Description of CVD synthesis of MoS<sub>2</sub> and STEM sample preparation, microscopy parameters, postacquisition reconstruction methods, simulation parameters, density functional theory calculations, supplementary figures (PDF)

## ■ AUTHOR INFORMATION

### Corresponding Author

\*E-mail: [Jamie.warner@materials.ox.ac.uk](mailto:Jamie.warner@materials.ox.ac.uk).

### ORCID

Jamie H. Warner: 0000-0002-1271-2019

### Notes

The authors declare no competing financial interest.

## ■ ACKNOWLEDGMENTS

J.H.W. thanks support from the European Research Council (Grant No. 725258). Y.W. thanks support from China scholarship council. Work at the Molecular Foundry was supported by the Office of Science, Office of Basic Energy Sciences, of the U.S. Department of Energy under Contract No. DE-AC02-05CH11231. We thank Diamond Light Source for access and support in use of the electron Physical Science Imaging Centre (Instrument E02 and proposal number MG22549) that contributed to the results presented here. S.F. and E.K. acknowledge support by the STC Center for Integrated Quantum Materials, NSF Grant No. DMR-1231319, and by ARO MURI Award No. W911NF-14-0247. The computations in this work were run on the Odyssey cluster supported by the FAS Division of Science, Research Computing Group at Harvard University. We thank Si Zhou for providing the TMD samples.

## ■ REFERENCES

- (1) Das, S.; Chen, H. Y.; Penumatcha, A. V.; Appenzeller, J. High performance multilayer MoS<sub>2</sub> transistors with scandium contacts. *Nano Lett.* **2013**, *13*, 100–105.
- (2) Wang, H.; Yu, L.; Lee, Y. H.; Shi, Y.; Hsu, A.; Chin, M. L.; Li, L. J.; Dubey, M.; Kong, J.; Palacios, T. Integrated Circuits Based on Bilayer MoS<sub>2</sub> Transistors. *Nano Lett.* **2012**, *12*, 4674–4680.
- (3) Lee, G. H.; Yu, Y. J.; Cui, X.; Petrone, N.; Lee, C. H.; Choi, M. S.; Lee, D. Y.; Lee, C.; Yoo, W. J.; Watanabe, K.; Taniguchi, T.; Nuckolls, C.; Kim, P.; Hone, J. Flexible and transparent MoS<sub>2</sub> field-effect transistors on hexagonal boron nitride-graphene heterostructures. *ACS Nano* **2013**, *7*, 7931–7936.
- (4) Zhai, C.; Zhu, M.; Bin, D.; Ren, F.; Wang, C.; Yang, P.; Du, Y. Two dimensional MoS<sub>2</sub>/graphene composites as promising supports for Pt electrocatalysts towards methanol oxidation. *J. Power Sources* **2015**, *275*, 483–488.

- (5) Hou, D.; Zhou, W.; Liu, X.; Zhou, K.; Xie, J.; Li, G.; Chen, S. Pt nanoparticles/MoS<sub>2</sub> nanosheets/carbon fibers as efficient catalyst for the hydrogen evolution reaction. *Electrochim. Acta* **2015**, *166*, 26–31.
- (6) Wang, T.; Zhu, R.; Zhuo, J.; Zhu, Z.; Shao, Y.; Li, M. Direct Detection of DNA below ppb Level Based on Thionin-Functionalized Layered MoS<sub>2</sub> Electrochemical Sensors. *Anal. Chem.* **2014**, *86*, 12064–12069.
- (7) Heiraniyan, M.; Farimani, A. B.; Aluru, N. R. Water desalination with a single-layer MoS<sub>2</sub> nanopore. *Nat. Commun.* **2015**, *6*, 1–6.
- (8) Schneider, G. F.; Kowalczyk, S. W.; Calado, V. E.; Pandraud, G.; Zandbergen, H. W.; Vandersypen, L. M. K.; Dekker, C. DNA translocation through graphene nanopores. *Nano Lett.* **2010**, *10*, 3163–3167.
- (9) Feng, J.; Liu, K.; Graf, M.; Lihter, M.; Bulushev, R. D.; Dumcenco, D.; Alexander, D. T. L.; Krasnozhan, D.; Vuletic, T.; Kis, A.; Radenovic, A. Electrochemical reaction in single layer MoS<sub>2</sub>: Nanopores opened atom by atom. *Nano Lett.* **2015**, *15*, 3431–3438.
- (10) Surwade, S. P.; Smirnov, S. N.; Vlassioun, I. V.; Unocic, R. R.; Veith, G. M.; Dai, S.; Mahurin, M. M. Water desalination using nanoporous single-layer graphene. *Nat. Nanotechnol.* **2015**, *10*, 459–464.
- (11) O'Hern, S. C.; Boutilier, M. S. H.; Idrobo, J. C.; Song, Y.; Kong, J.; Laoui, T.; Atieh, M.; Karnik, R. Selective ionic transport through tunable subnanometer pores in single-layer graphene membranes. *Nano Lett.* **2014**, *14*, 1234–1241.
- (12) Boutilier, M. S. H.; Jang, D.; Idrobo, J. C.; Kidambi, P. R.; Hadjiconstantinou, N. G.; Karnik, R. Molecular Sieving Across Centimeter-Scale Single-Layer Nanoporous Graphene Membranes. *ACS Nano* **2017**, *11*, 5726–5736.
- (13) Song, B.; Schneider, G. F.; Xu, Q.; Pandraud, G.; Dekker, C.; Zandbergen, H. Atomic-Scale Electron-Beam Sculpting of Near-Defect-Free Graphene Nanostructures. *Nano Lett.* **2011**, *11*, 2247–2250.
- (14) Robertson, A. W.; Lee, G. D.; He, K.; Gong, C.; Chen, Q.; Yoon, E.; Kirkland, A. I.; Warner, J. H. Atomic Structure of Graphene Subnanometer Pores. *ACS Nano* **2015**, *9*, 11599–11607.
- (15) Wang, S.; Li, H.; Sawada, H.; Allen, C. S.; Kirkland, A. I.; Grossman, J. C.; Warner, J. H. Atomic structure and formation mechanism of sub-nanometer pores in 2D monolayer MoS<sub>2</sub>. *Nanoscale* **2017**, *9*, 6417–6426.
- (16) Krajnak, M.; McGrouther, D.; Maneuski, D.; O'Shea, V.; McVitie, S. Pixelated detectors and improved efficiency for magnetic imaging in STEM differential phase contrast. *Ultramicroscopy* **2016**, *165*, 42–50.
- (17) Jiang, Y.; Chen, Z.; Han, Y.; Deb, P.; Gao, H.; Xie, S.; Purohit, P.; Tate, M. W.; Park, J.; Gruner, S. M.; Elser, V.; Muller, D. A. Electron ptychography of 2D materials to deep sub-Angström resolution. *Nature* **2018**, *559*, 343–349.
- (18) Krivanek, O. L.; Chisholm, M. F.; Nicolosi, V.; Pennycook, T. J.; Corbin, G. J.; Dellby, N.; Murfitt, M. F.; Own, C. S.; Szilagy, Z. S.; Oxley, M. P.; Pantelides, S. T.; Pennycook, S. J. Atom-by-atom structural and chemical analysis by annular dark-field electron microscopy. *Nature* **2010**, *464*, 571–574.
- (19) Close, R.; Chen, Z.; Shibata, N.; Findlay, S. D. Towards quantitative, atomic-resolution reconstruction of the electrostatic potential via differential phase contrast using electrons. *Ultramicroscopy* **2015**, *159*, 124–137.
- (20) Lazić, I.; Bosch, E. G. T.; Lazar, S. Phase contrast STEM for thin samples: Integrated differential phase contrast. *Ultramicroscopy* **2016**, *160*, 265–280.
- (21) Müller-Caspary, K.; Krause, F. F.; Grieb, T.; Löffler, S.; Schowalter, M.; Béché, A.; Galioit, V.; Marquardt, D.; Zweck, J.; Schattschneider, P.; Verbeeck, J.; Rosenauer, A. Measurement of atomic electric fields and charge densities from average momentum transfers using scanning transmission electron microscopy. *Ultramicroscopy* **2017**, *178*, 62–80.
- (22) Bates, R. H. T.; Rodenburg, J. M. Sub-Angström transmission microscopy: A fourier transform algorithm for microdiffraction plane intensity information. *Ultramicroscopy* **1989**, *31*, 303–307.

- (23) Rodenburg, J. M.; Bates, R. H. T. The theory of super-resolution electron microscopy via Wigner-distribution deconvolution. *Philos. Trans. R. Soc. London Ser. A Phys. Eng. Sci.* **1992**, 339, 521–553.
- (24) Yang, H.; Rutte, R. N.; Jones, L.; Simson, M.; Sagawa, R.; Ryll, H.; Huth, M.; Pennycook, T. J.; Green, M. L. H.; Soltau, H.; Kondo, Y.; Davis, B. G.; Nellist, P. D. Simultaneous atomic-resolution electron ptychography and Z-contrast imaging of light and heavy elements in complex nanostructures. *Nat. Commun.* **2016**, 7, 12532.
- (25) D'Alfonso, A. J.; Morgan, A. J.; Yan, A. W. C.; Wang, P.; Sawada, H.; Kirkland, A. I.; Allen, L. J. Deterministic electron ptychography at atomic resolution. *Phys. Rev. B: Condens. Matter Mater. Phys.* **2014**, 89, 064101.
- (26) Shibata, N.; Seki, T.; Sánchez-Santolino, G.; Findlay, S. D.; Kohno, Y.; Matsumoto, T.; Ishikawa, R.; Ikuhara, Y. Electric field imaging of single atoms. *Nat. Commun.* **2017**, 8, 15631.
- (27) Müller, K.; Krause, F. F.; Béch , A.; Schowalter, M.; Galioit, V.; L ffler, S.; Verbeeck, J.; Zweck, J.; Schattschneider, P.; Rosenauer, A. Atomic electric fields revealed by a quantum mechanical approach to electron picodiffraction. *Nat. Commun.* **2014**, 5, 5653.
- (28) Hachtel, J. A.; Idrobo, J. C.; Chi, M. Sub- ngstrom electric field measurements on a universal detector in a scanning transmission electron microscope. *Adv. Struct. Chem. Imag.* **2018**, 4, 10.
- (29) Ishikawa, R.; Findlay, S. D.; Seki, T.; S nchez-Santolino, G.; Kohno, Y.; Ikuhara, Y.; Shibata, N. Direct electric field imaging of graphene defects. *Nat. Commun.* **2018**, 9, 3878.
- (30) Griffiths, A. J. V.; Walther, T. Quantification of carbon contamination under electron beam irradiation in a scanning transmission electron microscope and its suppression by plasma cleaning. *J. Phys. Conf. Ser.* **2010**, 241, 012017.
- (31) Ennos, A. E. The origin of specimen contamination in the electron microscope. *Br. J. Appl. Phys.* **1953**, 4, 101–106.
- (32) Ennos, A. E. The sources of electron-induced contamination in kinetic vacuum systems. *Br. J. Appl. Phys.* **1954**, 5, 27–31.
- (33) Cowley, J. M.; Moodie, A. F. The scattering of electrons by atoms and crystals. I. A new theoretical approach. *Acta Crystallogr.* **1957**, 10, 609–619.
- (34) Goodman, P.; Moodie, A. F. Numerical evaluations of N-beam wave functions in electron scattering by the multi-slice method. *Acta Crystallogr., Sect. A: Cryst. Phys., Diffr., Theor. Gen. Crystallogr.* **1974**, 30, 280–290.
- (35) Ishikawa, R.; Okunishi, E.; Sawada, H.; Kondo, Y.; Hosokawa, F.; Abe, E. Direct imaging of hydrogen-atom columns in a crystal by annular bright-field electron microscopy. *Nat. Mater.* **2011**, 10, 278–281.
- (36) Shibata, N.; Findlay, S. D.; Matsumoto, T.; Kohno, Y.; Seki, T.; S nchez-Santolino, G.; Ikuhara, Y. Direct Visualization of Local Electromagnetic Field Structures by Scanning Transmission Electron Microscopy. *Acc. Chem. Res.* **2017**, 50, 1502–1512.
- (37) Muller, D. A.; Nakagawa, N.; Ohtomo, A.; Grazul, J. L.; Hwang, H. Y. Atomic-scale imaging of nanoengineered oxygen vacancy profiles in SrTiO<sub>3</sub>. *Nature* **2004**, 430, 657–661.
- (38) Johnston-Peck, A. C.; Winterstein, J. P.; Roberts, A. D.; DuChene, J. S.; Qian, K.; Sweeny, B. C.; Wei, W. D.; Sharma, R.; Stach, E. A.; Herzing, A. A. Oxidation-state sensitive imaging of cerium dioxide by atomic-resolution low-angle annular dark field scanning transmission electron microscopy. *Ultramicroscopy* **2016**, 162, 52–60.
- (39) Johnson, J. M.; Im, S.; Windl, W.; Hwang, J. Three-dimensional imaging of individual point defects using selective detection angles in annular dark field scanning transmission electron microscopy. *Ultramicroscopy* **2017**, 172, 17–29.
- (40) Yu, Z.; Muller, D. A.; Silcox, J. Study of strain fields at a-Si/c-Si interface. *J. Appl. Phys.* **2004**, 95, 3362–3371.
- (41) Grillo, V.; Rossi, F. A new insight on crystalline strain and defect features by STEM-ADF imaging. *J. Cryst. Growth* **2011**, 318, 1151–1156.
- (42) Fang, S.; Wen, Y.; Allen, C. S.; Ophus, C.; Han, G. G. D.; Kirkland, A. I.; Kaxiras, E.; Warner, J. H. Atomic electrostatic maps of 1D channels in 2D semiconductors using 4D scanning transmission electron microscopy. *Nat. Commun.* **2019**, 10, 1–9.